ARTICLE

# Passive targeting of high-grade gliomas via EPR effect: a closed path for metallic nanoparticles?

Received 00th January 20xx,
Accepted 00th January 20xx

DOI: 10.1039/x0xx00000x

Carlos Caro,[a] Ashish Avasthi,[a] Jose M. Paez-Muñoz,[a] Manuel Pernía-Leal,*[b] and Maria L. García-Martín*[a,c]

Passive tumor targeting via enhanced permeability and retention (EPR) effect has long been considered the most effective mechanism for the accumulation of nanoparticles inside solid tumors. However, several studies have demonstrated that the EPR effect is largely dependent on the tumor type and location. Particularly complex is the situation in brain tumors, where the presence of the blood-brain tumor barrier (BBTB) adds an extra limiting factor in reaching the tumor interstitium. However, it remains unclear whether these restraints imposed by the BBTB prevent the EPR effect from acting as an efficient tumor targeting mechanism for metallic nanoparticles. In this work, we have studied the EPR effect of metallic magnetic nanoparticles (MMNPs) in a glioblastoma (GBM) model by parametric MRI. Our results showed that only MMNPs ≤ 50 nm could reach the tumor interstitium, whereas larger MMNPs were unable to cross the BBTB. Furthermore, even for MMNPs around 30-50 nm, the amount of them found within the tumor was scarce and restricted to the vicinity of large tumor vessels, indicating that the BBTB strongly limits the passive accumulation of metallic nanoparticles in brain tumors. Therefore, active targeting becomes the most reasonable strategy to target metallic nanoparticles to GBMs.

## Introduction

Glioblastoma multiforme (GBM) is the most common primary malignant brain tumor, responsible for 15% of all brain-tumor diagnoses worldwide, exhibiting very aggressive behavior and poor prognosis.[1] The median survival of GBM patients following diagnosis is only about 15 months, with less than 5% of patients surviving more than five years.[2, 3] GBM represents 50% of all gliomas, if we consider all age groups, since, although the highest incidence is between 55 and 60 years, GBM can affect people of any age.[4] Regarding GBM diagnosis, it relies on neuroimaging exams, mainly Magnetic Resonance Imaging (MRI), followed by histological confirmation.[5] MRI is a powerful technique with many remarkable advantages, such as its non-invasive character, the use of non-ionizing radiation, its excellent image quality, and its ability to provide both anatomical and functional information.[6] However, despite the advantages mentioned above, the specificity of MRI in tumor diagnosis is limited, and the use of contrast agents (CAs) is often required for the proper visualization of the tumor.[7] The vast majority of the CAs currently used in clinical MRI are chelates of the paramagnetic gadolinium (III) ions.[8] These Gd-chelates have several limitations, namely, toxicity issues related to the unexpected release and tissue deposition of $Gd^{3+}$,[9-11] and lack of diagnostic specificity, since the signal enhancement they produce in tumors is simply due to the extravasation of the CA through the more permeable angiogenic vessels.[12] As for the treatment, given that GBM is a very fast-growing and highly infiltrating tumor, very aggressive therapy is usually chosen, based on surgical resection, followed by radiotherapy and chemotherapy. But even with such aggressive treatment, the 5-year survival rate remains very low, as mentioned above.[13] Therefore, there is an urgent need to improve the therapeutic efficacy of GBM treatments and the diagnostic specificity of *in vivo* imaging. Some of the more recent approaches to tackle this problem have emerged from nanotechnology. In the 21st Century, nanotechnology has undergone a vigorous development that has opened up new and promising horizons in several different fields, including nanomedicine.[14-16] In particular, nanoparticles (NPs) have emerged as promising tools to overcome current limitations in cancer diagnosis and treatment.[17-19] In this sense, metallic magnetic nanoparticles (MMNPs) have attracted a great deal of attention due to their wide range of applications in tumor theranostics. MMNPs can be used as CAs for MRI, as heating mediators in magnetic hyperthermia, or as drug-delivery carriers.[20, 21] However, a critical aspect that has been limiting their applicability *in vivo* is the ability of these nanomaterials to reach and accumulate in the tumor efficiently.[22] Passive tumor targeting through the enhanced permeability and retention (EPR) effect, first described by Maeda and Matsumura in 1986,[23] has long been considered the prevalent and most effective mechanism that governs the accumulation of small, long-circulating NPs inside solid tumors.[24-26] The EPR effect relies on the increased leakiness of the tumor vasculature and poor lymphatic drainage, leading to intratumoral accumulation and retention of NPs .[27, 28] Tumor vasculature is formed rapidly, driven by the tumor growth rate, hypoxia, growth factors, among others, leading to immature vessels with fenestrations that allow the extravasation of relatively large

[a] BIONAND – Centro Andaluz de Nanomedicina y Biotecnología (Junta de Andalucía-Universidad de Málaga), C/ Severo Ochoa, 35, 29590 Málaga, Spain.
[b] Departamento de Química Orgánica y Farmacéutica, Facultad de Farmacia, Universidad de Sevilla, 41012 Sevilla, Spain.
[c] Biomedical Research Networking Center in Bioengineering, Biomaterials & Nanomedicine (CIBER-BBN).

† Footnotes relating to the title and/or authors should appear here.
Electronic Supplementary Information (ESI) available: [details of any supplementary information available should be included here]. See DOI: 10.1039/x0xx00000x

particles. The cutoff size of these fenestrations determines the maximum size of the particles that can extravasate into the tumor interstitium.[29] Indeed, the size dependence of the EPR effect has been extensively studied in preclinical models, showing efficient tumor targeting for NPs ranging from 12 to 200 nm.[30-32] NPs outside this range would be rapidly cleared from the bloodstream, either by the kidneys, if they are smaller, or by the mononuclear phagocyte system (MPS), if they are larger.[33] The situation is more complex in brain tumors, where the EPR effect encounters an additional obstacle, the blood-brain barrier (BBB).[34] The BBB is formed by endothelial cells connected by tight junctions that create a highly restrictive barrier that protects the central nervous system from infectious agents and toxins. This barrier is compromised during tumor progression, especially in high-grade tumors such as GBM, resulting in a leaky vasculature known as the blood-brain tumor barrier (BBTB). However, the BBTB is highly heterogeneous, exhibiting non-uniform vascular permeability, which directly affects the EPR effect in GBM. Thus, according to the studies by Sarin et al.,[35, 36] using organic NPs (polyamidoamine dendrimers), the pore size upper limit of the neoplastic capillaries of malignant brain tumors is around 12 nm. However, Schlageter et al.,[37] who studied the microvessel structure in brain tumor models using electron microscopy, reported pore sizes around 50 nm, and the existence of endothelial gaps of about 1.1 μm. But not only the size of NPs is important for passive tumor targetting, other aspects, such as lipophilicity, stiffness, and above all, blood circulation times are also critical.[38] Indeed, most papers claiming an efficient EPR effect of nanomaterials in brain tumors refer to liposomes[39-41] or polymeric NPs,[42, 43] whereas no conclusive evidence of such effect has been reported so far for MMNPs. Thus, the main goal of this work was to evaluate the ability of metallic NPs, which exhibit substantially higher stiffness than liposomes or polymeric NPs, to passively reach the tumor interstitium of high-grade gliomas. MRI offers unique advantages for the *in vivo* evaluation of the EPR effect of MMNPs since it can simultaneously assess the biodistribution and pharmacokinetics of MMNPs, along with tumor vascular permeability. Here, we report a detailed study on the ability of long-circulating PEGylated iron oxide NPs, previously reported by us,[44] to passively target GBM via EPR effect. To this end, we produced NPs with hydrodynamic diameters (HD) ranging from 30 to 70 nm, in physiological conditions. These MMNPs were administered intravenously in rats bearing orthotopic C6 gliomas and followed by quantitative MRI for up to 24 h. Furthermore, MMNPs distribution within the tumors was assessed histologically in tissue sections, and the blood residence time determined by relaxometry. Only MMNPs below 50 nm HD were able to cross the BBTB and accumulate in the tumor interstitium, albeit very inefficiently, with small amounts of MMNPs found only nearby large tumor blood vessels. These findings strongly suggest that passive targeting via the EPR effect is insufficient for efficient delivery of MMNPs to malignant brain tumors, leading to active transport as the most plausible strategy to achieve successful targeting.

## Results and discussion

### Characterization of nanoparticles

In this work, three different iron oxide magnetic NPs were synthesized, hereinafter referred to as MMNP1, MMNP2, and MMNP3. As can be observed in Figure 1, MMNP1 and MMNP2 showed cubical shape, and 7 and 20 nm in size, respectively, whereas MMNP3 exhibited spherical shape and 22 nm in size (Figure 1a-f). We used different ratios of Fe precursor:oleic acid (MMNP1=5:2, MMNP2=2:1, and MMNP3=0.2:10), resulting in differences in the size or shape of the NPs, in agreement with previous studies by Park et al.,[45] who reported that the morphology of magnetic NPs could be fine-tuned on demand by varying the precursor to solvent ratio. However, we realized that other parameters, such as heating ramp and stirring, affected the final result drastically. Overall, we concluded that an increase in the temperature ramp from 1°C/min to 3°C/min, high Fe precursor to oleic acid ratios, and low stirring promoted more homogenous growing and larger sizes of the MMNPS. Therefore, we followed this strategy to obtain NPs of different sizes. To render highly water stable and monodisperse nanoconjugates, MMNPs were functionalized with strong binding ligands based on a gallol group as anchor and PEG molecules as solubilizing agents. MMNP1 was functionalized with gallol-PEG1.5kDa-OH, while MMNP2 and MMNP3 were functionalized with gallol-PEG3kDa-OH.[46] The size of PEG was selected according to previous studies reported by us.[44] The presence of the gallol-PEG ligand at the nanoparticle surface was confirmed by FTIR spectroscopy, being able to assign the main peaks of the ligand in the corresponding functionalized-MMNPs (Figure S1). To prove the proper functionalization and, consequently, to demonstrate the high stability of these MMNPs, the hydrodynamic diameters (HD) were measured by DLS. MMNP1 showed an HD around 24 nm in water, which slightly increased in PBS (31nm) and FBS (34nm). The same trend was observed for MMNP2 and MMNP3, HDs of 34 nm and 45 nm respectively in water, 46 nm and 62 nm in PBS, and 51 nm and 71 nm in FBS (Figure 1d-f, Figure S2). Moreover, the stability of the MMNPs under physiological conditions was studied by measuring the HD diameters in FBS for 168h, resulting in very similar values throughout this time (Figure 1g). The zeta potentials of MMNPs were also measured, being -8.2 mV for MMNP1, -13.4 mV for MMNP2, and -15.0 mV for MMNP3, which also explains the high stability in biological media (Figure 1h).[47]

The transverse relaxivities ($r_2$) determined at high magnetic field (9.4T) were 136.5 $mM^{-1}•s^{-1}$, 153.6 $mM^{-1}•s^{-1}$, and 54.3 $mM^{-1}•s^{-1}$ for MMNP1, MMNP2, and MMNP3, respectively (Figure S3). MMNP1 and MMNP2 values were in good agreement with previously reported results for similar magnetic nanoparticles.[48] As for the lower $r_2$ values of MMNP3, they can be explained by differences in the anisotropy of the core, which directly affects the Néel relaxation.[49]

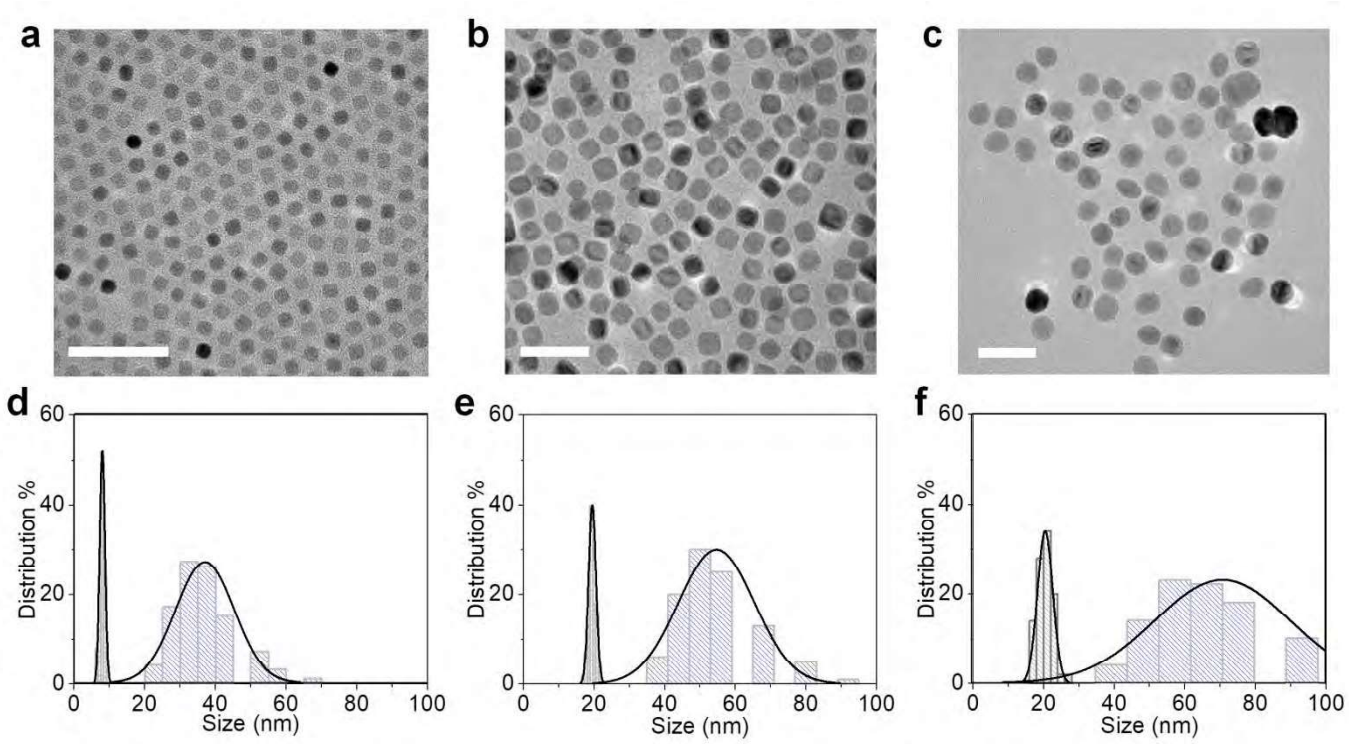


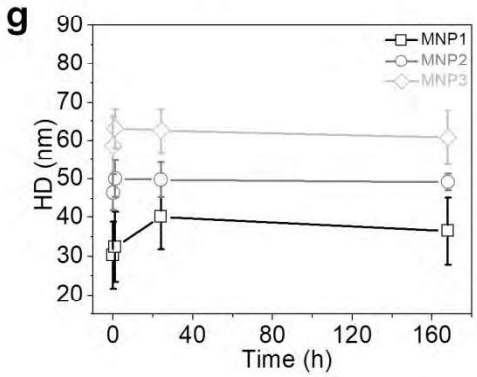


h

| | MMNP1 | MMNP2 | MMNP3 |
|---|---|---|---|
| $D_{TEM}$ (nm) | 8.0 ± 0.7 | 20.3 ± 1.8 | 22.3 ± 3.1 |
| HD (nm) | 34.3 ± 8.1 | 51.7 ± 1.0 | 71.4 ± 2.1 |
| ζ (mV) | -8.2 | -13.4 | -15.0 |
| $r_2$ ($mM^{-1}•s^{-1}$) | 136.5 (92.1) | 153.6 (105.3) | 54.3 (40.2) |

**Fig. 1.** Physicochemical characterization of MMNPs. TEM images and the corresponding size distribution histograms of MMNP1 (a, d),

MMNP2 (b, e), and MMNP3 (c, f). Scale bar corresponds to 50 nm in all cases. g) HDs of the three MMNPs determined in FBS at different times using DLS. h) Summary table containing the core diameter of the three MMNPs measured by TEM ($D_{TEM}$), the HD determined by DLS, the zeta potential ($\zeta$), and the transverse relaxivity ($r_2$) at 9.4 T and 1.44 T (in brackets).

**Cytotoxicity assessment**

An exhaustive cytotoxicity evaluation was performed in N13 cells, including mitochondrial activity assays, cell cycle analysis, cell morphology evaluation, and live-dead experiments. The MTT assay showed no significant effect on the mitochondrial activity of any of the NPs for concentrations up to 50 µg/mL, and only MMNP3 showed some effect at the highest concentration tested (100 µg/mL) (Figure 2a). On the other hand, the evaluation of the cell cycle showed that cells exposed to MMNP1 and MMNP2 kept the proportion of cells in the different phases of the cell cycle ($G_0/G_1$-S-$G_2$/M) virtually identical to the negative control at any of the concentrations tested. On the contrary, MMNP3 at concentrations above 50 µg/mL altered the cell cycle preventing cells from progressing from $G_1$ to S phase (significant $p<0.05$) and even inducing some apoptosis (sub$G_0$) (Figure 2b and S4). Likewise, the live-dead assay and the evaluation of cell morphology by optical images showed absence of cytotoxicity of all three MMNPs for concentrations up to 50 µg/ml, and only MMNP3, at the highest concentration tested (100 µg/ml), induced changes in the morphology of cells (Figures 2c-2f and S5), a decrease in the total number of cells (Figure 2g), but no changes in dead cell percentage (Figure 2h). The moderate cytotoxic effects caused by MMNP3 at high concentrations can be related to higher uptake efficiency by cells due to the larger size of these MMNPs, as previously shown by Wu *et al.*[50] In conclusion, the exhaustive cytotoxicity evaluation demonstrates the biosafety of all MMNPs for concentrations as high as 50 µg/mL, which is well above the expected *in vivo* cellular exposure concentration for the amount of MMNPs injected in the *in vivo* experiments.

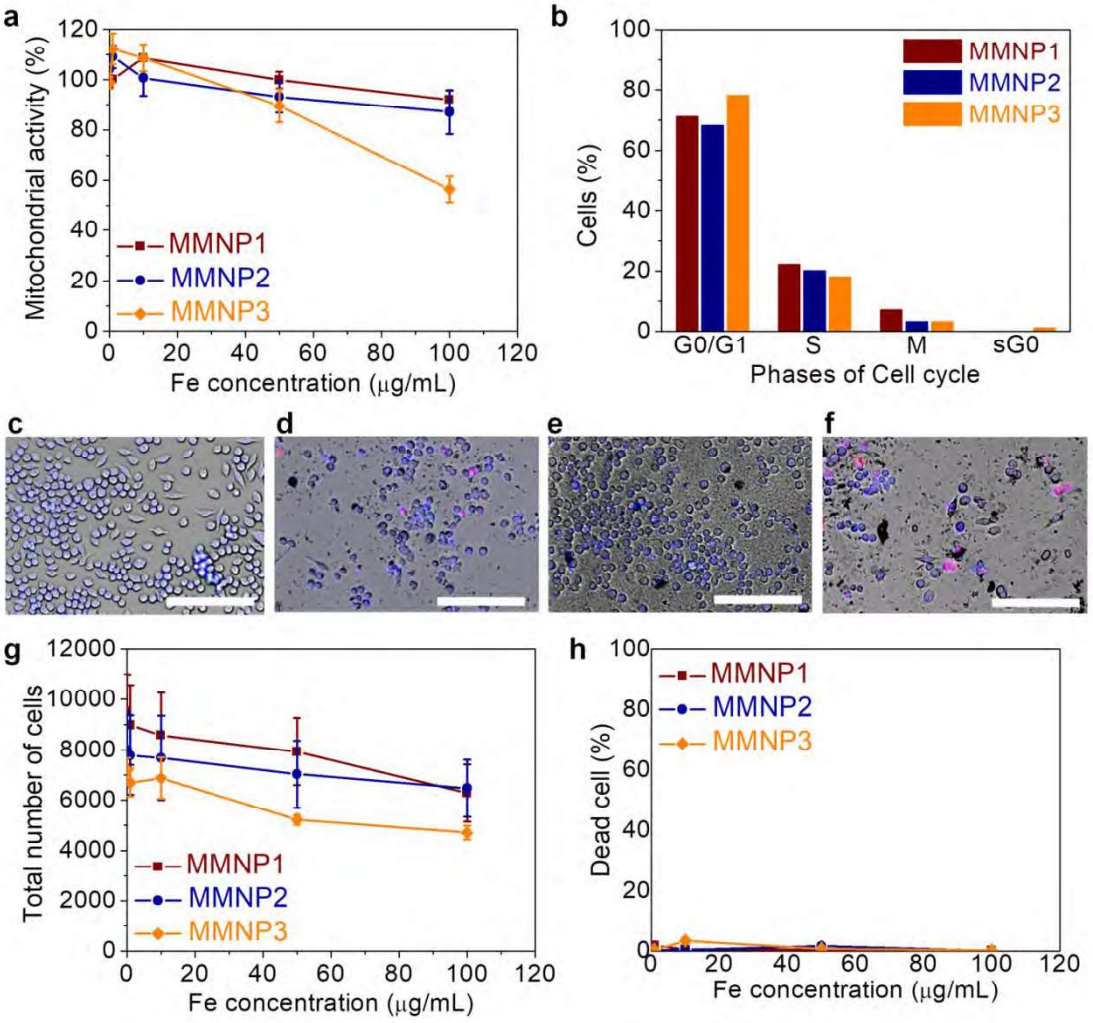

**Fig. 2.** Cytotoxicity evaluation of MMNPs on N13 cells. a) MTT assay after 24 h exposure to growing concentrations of MMNPs. b) Flow cytometry analysis of cell cycle after 24 h of exposure to MMNP. Images of the cultured cell exposed to PBS (c), MMNP1 100 µg/mL (d), MMNP2 100 µg/mL (e), MMNP3 100 µg/mL (f). The images show the merge of brightfield (grey), DAPI (blue) and TO-PRO-3 Iodine (red). The scale bar corresponds to 100 µm. Live-dead assay: total amount of cell, by counting nuclei stained with DAPI (g), percentage of dead cells, by calculating nuclei stained with DAPI and PI (h).

***In vivo* MRI studies**

Once the MMNPs were characterized physicochemically and biologically *in vitro*, their capacity to target brain tumors via the EPR effect was evaluated *in vivo* by MRI using an orthotopic model of GBM. First, short-term pharmacokinetics (PKs), over the first 30 min, were calculated by semi-quantitative analysis of dynamic $T_2$ MRI experiments.[51] The relative intensity to the contralateral healthy brain showed that MMNP1 and MMNP2 produced a slight continuous signal decay up to the end of the experiment, being a little more pronounced for MMNP1 (Figure 3a,b), whereas MMNP3 did not induce any signal change (Figure 3c). These results suggest that only a small amount of MMNP1 and MMNP2 entered the tumor during this short period of time, while MMNP3 did not enter at all. Since the ability of any compound to reach the tumor depends, in the first place, on the tumor vascular permeability, we performed $T_1$ dynamic contrast-enhanced (DCE) MRI using a commercial Gd-chelate (Gadovist, Schering AG, Berlin, Germany) to evaluate such permeability in our tumor model. After the intravenous injection of the Gd-chelate, a rapid signal enhancement was observed, in agreement with the expected extravasation of small CAs into the tumor interstitium (Figure 3d). This rapid signal increase was followed by a slow signal decay, corresponding to the clearance of the Gd-chelate from the tumor. These pharmacokinetic profiles demonstrate the high vascular permeability of our tumor model and are in good agreement with those reported for human GBMs.[52] Therefore, the short pharmacokinetics studies show, on the one hand, that the BBTB of our C6 tumor model exhibit the high expected permeability of high-grade gliomas, and, on the other hand, that despite this high vascular permeability, MMNPs ranging from 30 to 70 nm can barely cross the BBTB and reach the tumor interstitium during this time window.

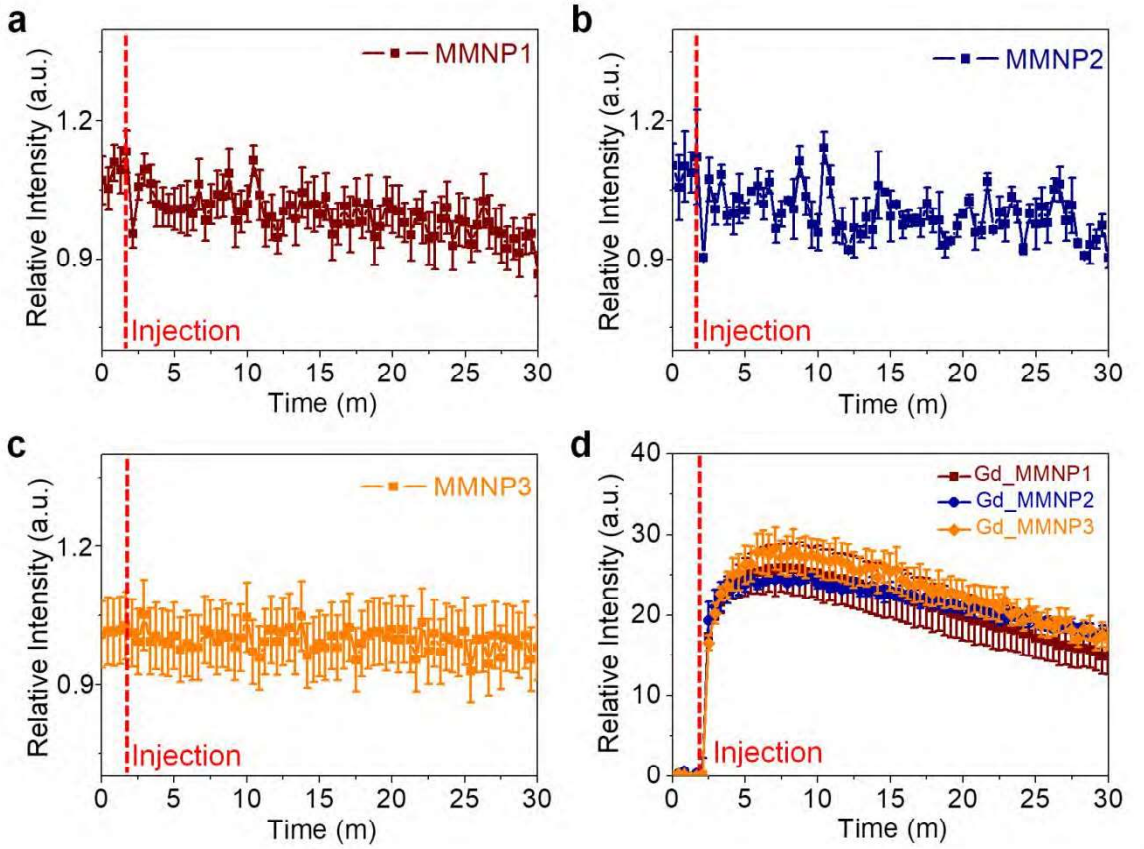


**Fig. 3.** Short-term MRI pharmacokinetics of MMNP1 (a), MMNP2 (b), MMNP3 (c) and Gadovist (d) in orthotopic C6 glioma tumors. The relative intensity corresponds to the ratio of the tumor signal divided by the signal from the healthy contralateral parenchyma**.**

Then, to evaluate the passive tumor targeting of our MMNPs via the EPR effect, we conducted long-term pharmacokinetics studies by morphological and parametric MRI (Figure 4). The high-resolution $T_2$-weighted MR images in Figure 4a show very subtle contrast

changes at 1h and 24 h after the injection of MMNP1 and MMNP2, which can be better appreciated in the parametric $T_2$ maps (Figure 4c), where a ring-shaped darkening appears at the periphery of the tumor due to the decrease in $T_2$ mediated by MMNPs. On the contrary, no changes could be observed for MMNP3, neither in the morphological nor in the parametric $T_2$ images, indicating that these MMNPs could not reach the tumor interstitium even at 24h, that is, they could not passively target the tumor. Conversely, $T_1$-weighted images (Figure 4b) and time-to-peak (TTP) parametric images (Figure 4d) acquired after injection of the Gd-chelate showed a strong contrast change with the typical enhancement pattern of GBMs,[53] characterized by high and rapid Gd uptake at the periphery of the tumor, and slight and slow uptake at the center of the tumor, corresponding to the well-vascularized and necrotic parts, respectively. Indeed, several studies have shown the correlation between DCE-MRI-derived parameters and tumor neovascularization patterns using immunohistochemistry.[54, 55] Therefore, the low penetrability of the MMNPs into the tumor could not be attributed to the absence of tumor vascularization but to the restrictive permeability of the BBTB, which allowed small molecules, such as the Gd-chelates, to readily extravasate, whereas it hampered the passage of the larger MMNPs.

**Fig. 4.** Evaluation of passive tumor targeting by parametric MRI. a) $T_2$-weighted high-resolution MR images acquired at 0h, 1h, and 24h following the intravenous injection of MMNPs (10 mg Fe /kg). b) Average $T_1$-weighted MR images of the first 5 minutes after the

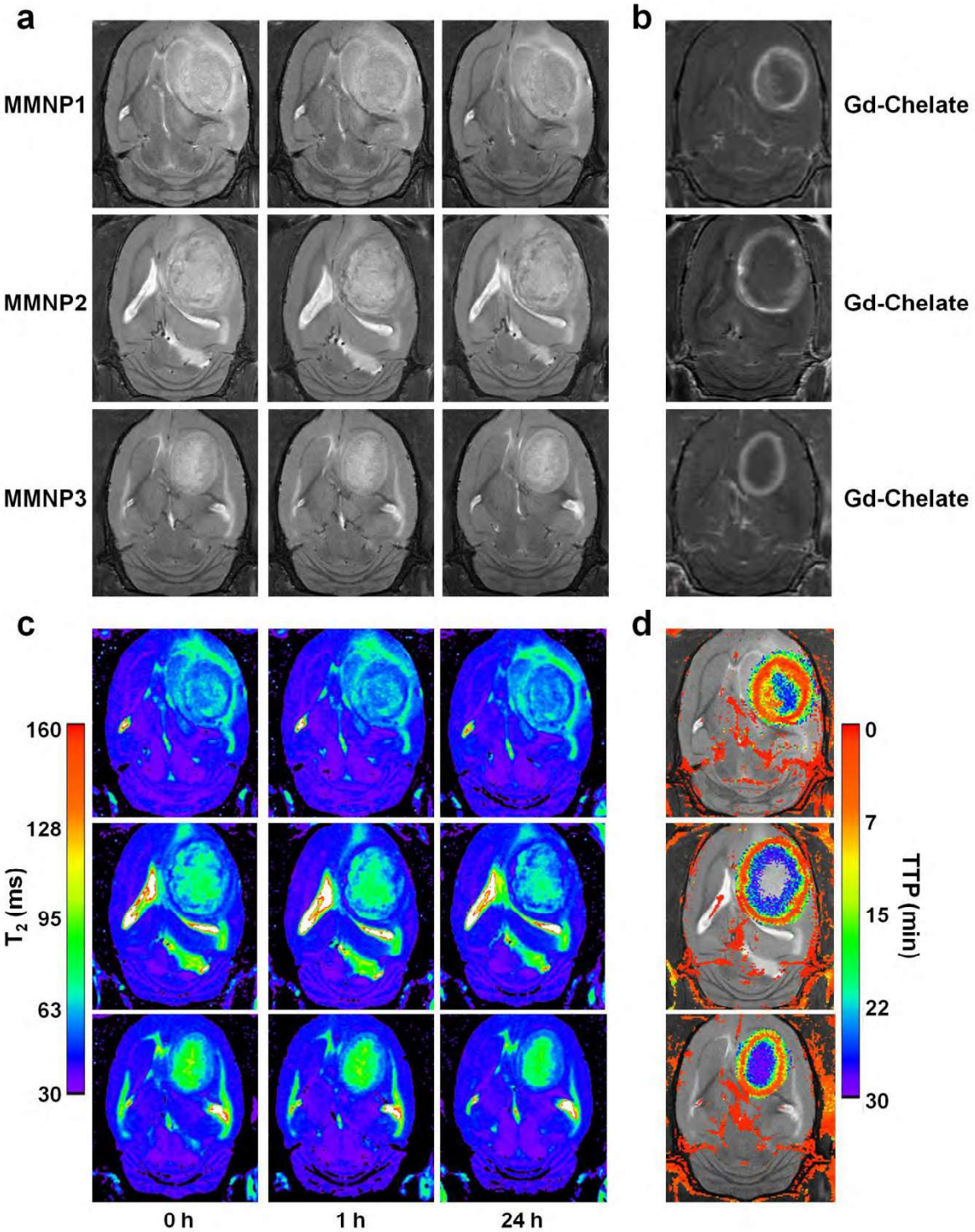

intravenous injection of Gadovist (0.1 mmol/kg). c) Parametric $T_2$ maps corresponding to the same animals and slices shown in (a). d) Time to peak (TTP) images calculated from the DCE-MRI measurements in (b), overlaid on $T_2$-weighted images for better visualization.

The quantitative analysis of these data is shown in Figure 5, where the mean transverse relaxation rate, $R_2$ ($1/T_2$), was calculated in the periphery of the tumor, using the TTP maps as a reference, over the entire tumor, and in the contralateral healthy parenchyma. Small but significant changes of $R_2$ were obtained in the tumor at 1 h post-injection of MMNP1 and MMNP2, with a $\Delta R_2$ of 0.8 $s^{-1}$ and 1.7 $s^{-1}$ respectively, whereas in the case of MMNP3, there were no significant differences between the $R_2$ values in the tumor and the contralateral part. Importantly, $\Delta R_2$ was significantly higher at 24 h post-injection of MMNP1 ($\Delta R_2$ of 1.7 $s^{-1}$) and even higher in the case of MMNP2 ($\Delta R_2$ 3.1 $s^{-1}$), as compared to 0 h and 1 h. On the contrary, no significant differences in $R_2$ were observed for MMNP3 at any experimental time. As expected, the changes in $R_2$ were larger in the periphery of the tumor (Figure 5a), corresponding to very short TTP values (Figure 4d), which are known to correlate with vascular density and/or permeability.[54] In other words, MMNPs accumulated in areas of tumors that are well vascularized and highly permeable. Accordingly, the average $R_2$ changes over the entire tumor were smaller (Figure 5b) due to the effect of the necrotic core of the tumor, where not even the Gd chelate could arrive efficiently, as shown by the long TTP values (Figure 4d). Interestingly, MMNP2 showed higher accumulation than MMNP1 at 1 h and 24 h, despite the fact that MMNP1 showed a more pronounced entry into the tumor during the first 30 min post-injection (Figure 3), suggesting that MMNP2 are retained in the tumor interstitium more efficiently, thus favoring the EPR effect for these MMNPs.

In summary, our results show that only MMNPs with sizes around 50 nm or below can passively accumulate in GBM, whereas MMNPs with sizes ≥ 70 nm cannot cross the BBTB. These results are in agreement with the 50 nm pore size of brain tumor microvessels reported by Schlageter *et al.*[37] Our data also suggest that although smaller MMNPs can more easily cross the BBTB, they are also more quickly cleared from the tumor, resulting in a less efficient EPR effect. But more importantly, our data show that even for MMNPs around 30-50 nm, the EPR effect in GBMs is very inefficient, allowing MMNPs to reach very small concentrations within the tumor, which very likely are insufficient for diagnostic or therapeutic applications. This is in line with clinical outcomes from anticancer drug delivery nanosystems, which have cast doubt on the efficacy of the EPR effect to target tumors passively,[56] particularly brain tumors.[57]

On the other hand, other studies have reported positive results regarding passive targeting of NPs to GBMs with nanomaterials. However, in most cases, these studies referred to soft NPs, such as liposomal or polymeric NPs.[30, 31, 39, 40] This higher EPR effect efficiency is very likely related to the higher elasticity of soft NPs, which has been demonstrated to play a critical role in cell and tumor uptake.[58, 59]

Therefore, not only the presence of BBTB, but also the stiffness of MMNPs may be a major factor underlying the inability of these NPs to effectively target tumors via EPR effect.

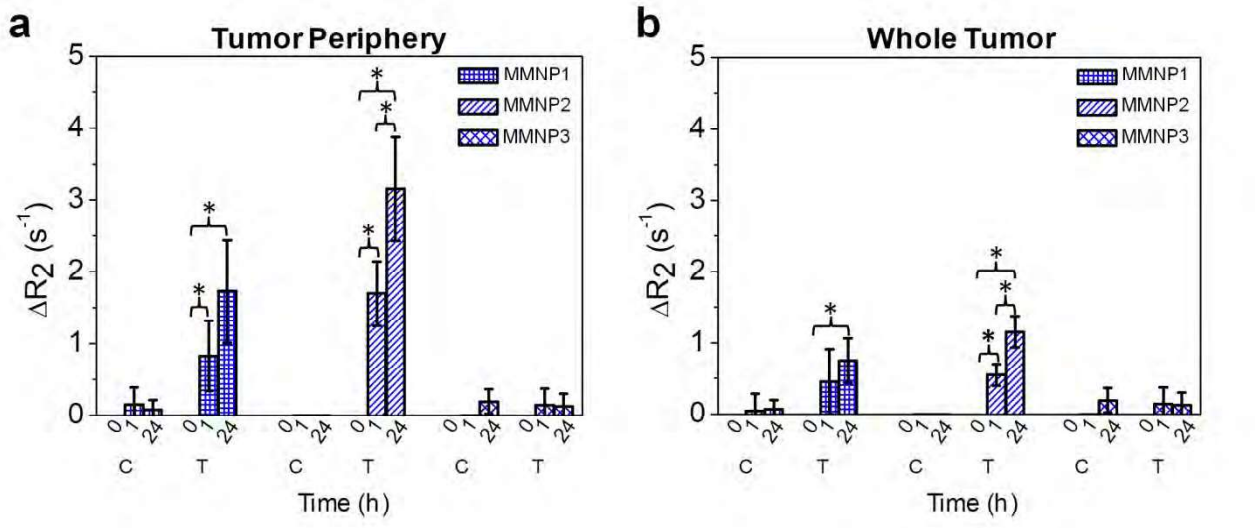


**Fig. 5.** Quantification of the average changes (n=4) in the transverse relaxation rate ($R_2$) in the tumor periphery (a) and over the entire tumor (b), at 1 and 24 h after the intravenous injecton fo MMNPs (10 mg Fe /kg). C and T correspond to contralateral and tumor, respectively. The star indicates significant differences ($\alpha$ = 0.05).

**Histological analysis**

Brain sections containing the tumor were stained with Hematoxylin and Eosin (H&E) to determine their microanatomy and with Prussian blue (PB) to detect the presence of MMNPs. As expected, C6 tumors showed high cellularity, dense cell packing, and high vascularization, with wide blood vessels evidenced by the presence

of red blood cells (Figure 6a-c).[60, 61] On the other hand, PB staining, which reacts with colloidal iron from MMNPs, revealed the presence of MMNP1 and MMNP2 within the tumor interstitium, thus demonstrating that these MMNPs were able to passively cross the BBTB, although very inefficiently, being only detectable in the vicinity of the major blood vessels (Figure 6d,e), were the presence of larger fenestrations likely allowed these NPs to go through. As for the MMNP3, they could not be detected at all (Figure 6f), indicating that these MMNPs were not able to cross the BBTB. These data support the conclusions derived from the *in vivo* MRI studies, which indicate, on the one hand, that the cutoff size for passive tumor targeting of MMNPs is around 50 nm, and, on the other hand, that the EPR effect is not sufficient to achieve efficient delivery of MMNPs to brain tumors. Histological evaluation of liver, spleen, kidney and liver was also conducted after 24 hours of exposure to MMNPs to assess their potential in vivo toxicity (Figure S6). Normal histological architecture was observed in all cases, in the absence necrotic foci, inflammatory cells, edema or any other sign of toxicity. Therefore, the systemic administration of MMNPs did not produce any detectable tissue alteration related to toxicity in the main organs.

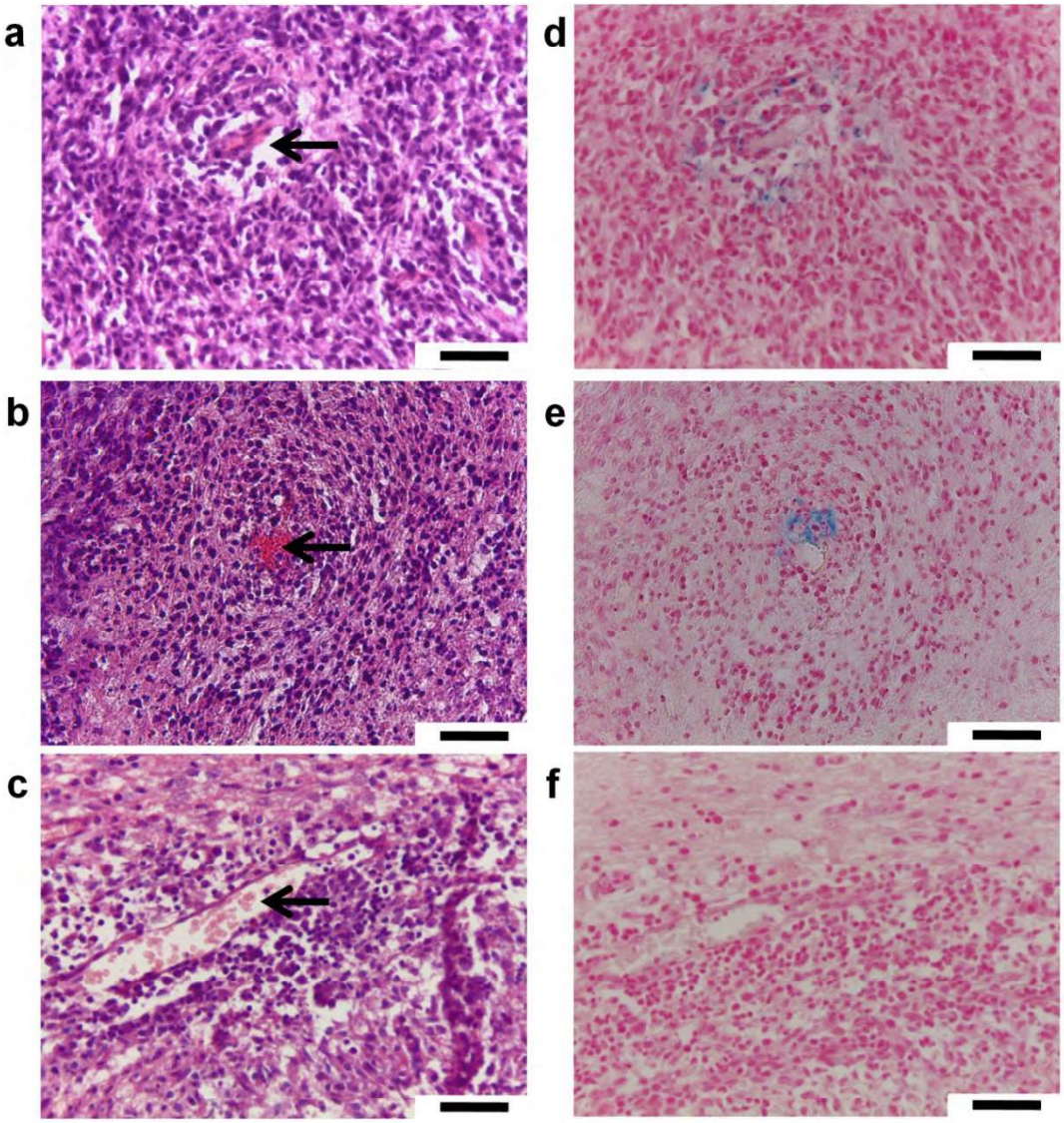


**Fig. 6**. Representative histological sections of H&E staining of tumors at 24h post injection of`MMNP1 (a), MMNP2 (b) and MMNP3 (c). Arrows indicate the main blood vessels. Representative histological sections of PB staining of the same tumors: MMNP1 (d), MMNP2 (e) and MMNP3 (f). The scale bar corresponds to 50 μm.

**Blood analysis**

Additionally, the long-circulating nature of our MMNPs, which was expected according to previous results reported by us,[44] was assessed by analyzing blood plasma samples at 1 h and 24 h after intravenous injection of MMNPs by TEM and relaxometry (Figure 7). TEM images clearly showed the presence of a large amount of MMNPs in plasma at 1h, which, although at a much lower concentration, were still present at 24 h (Figure 7a). Then, the

concentration of MMNPs in the blood was calculated from the transverse relaxation rate ($R_2$) estimated in the blood plasma at 1 h and 24 h using the relaxivity values obtained in vitro at 1.44 T (Figure S3), and the percentage of MMNPs to the injected dose was calculated using estimated blood volumes according to published data (Figure 7b).[62] The results confirmed the high concentration of MMNPs present at 1 h after their intravenous administration, with relative concentrations ranging from 22% to 46% of the injected dose. Finally, the concentration of MMNPs at 24 h was very low in all cases, in agreement with the TEM images, although still detectable. These results demonstrate that our MMNPs remain in circulation for several hours, which should promote tumor accumulation if the EPR effect worked as an efficient mechanism in brain tumors. However, as discussed above, none of the MMNPs exhibited substantial passive tumor targeting, which in principle could be attributable to the restrictions imposed by the BBTB,[63] although very likely there are other factors involved. Indeed, there is a strong criticism highlighting the importance of several factors that would hinder the transport of nanometric systems through the tumor microenvironment and limit their arrival to the numerous tumor cells far from active blood vessels. Among these factors are the high tumor interstitial fluid pressure (TIFP), the heterogeneous blood supply, or the impossibility to diffuse to avascular regions.[56, 64] Our

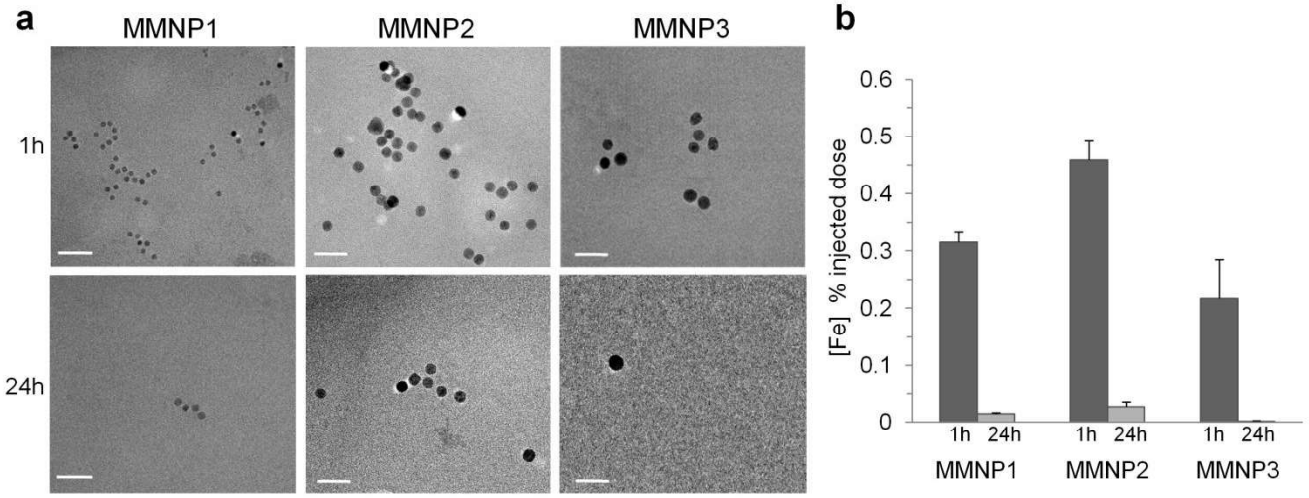


**Fig. 7**. Representative TEM images of blood samples at 1 h and 24 h after MMNPs injection (a). Iron percentage at 1 h and 24 h post MMNPs administration calculated based on 1.44 T relaxivity values (b).

## Experimental Section

### Materials

Chemicals and solvents were purchased to commercial suppliers (Acros Organics and Fisher Scientific, Sigma Aldrich) and used as received. Iron (III) chloride, Sodium Oleate, Oleic acid 99%, Gallic acid, Poly ethylene glycol 1500 Da, Poly ethylene glycol 3000 Da, 1-octadecene, Triethylamine, dicyclohexyl carbodiimide, 4-Dimethylaminopyridine, Hydrochloric acid, Sodium sulfate, Phosphate Buffered Saline (PBS), 3-[4,5-dimethylthiazol-2yl]-2,5-diphenyl tetrazolium bromide (MTT), Roswell Park Memorial Institute (RPMI), Dulbecco's Modified Eagle's Medium (DMEM). Milli-Q water (18.2 MΩ, 0.22µM filter por size) from Millipore. Toluene, ethanol, acetone, hexane, dimethylsulphoxide, chloroform, dichloromethane and tetrahydrofuran were used anhydrous and HPLC grade.

### Synthesis of the Nanoparticles

**Synthesis of Iron Oleate.** The synthesis was done following a published procedure.[45] Complete information about this protocol is provided in the supporting information.

**Synthesis of MMNP1.** 4.5g (5 mmol) of the previously prepared iron oleate and 0.57g (2 mmol) of oleic acid were solved in 20g of 1-octadecene. The mixture was heated up to a temperature of 320 °C following a heating ramp of 3 °C/min. Once this temperature was reached, it was maintained for 1 h and then cooled down to room temperature. Additionally, a purification of the NPs: first, NPs were washed several times, adding acetone-ethanol (ratio 1:1) in order to precipitate them; after that, they were centrifuged at 5.000 rpm for 10min; and finally, the NPs were suspended in toluene.

**Synthesis of MMNP2.** 1.8g (2 mmol) of the previously prepared iron oleate and 0.285g (1 mmol) of oleic acid were solved in 15g of 1-octadecene. This solution was heated to 200 °C under inert atmosphere, and subsequently raised to 320 °C with a heating ramp

of 1 °C / min. The synthesis was maintained at that temperature for 1h, and then the reaction was cooled down. Then, the same protocol described for MMNP1 was performed. Finally the MMNP2 were suspended in toluene.

**Synthesis of MMNP3.** 0.18g (0.2 mmol) of the previously prepared iron oleate and 2.84g (10 mmol) of oleic acid were solved in 5g of 1-octadecene. This solution was heated to 320 °C under inert atmosphere. The synthesis was maintained at that temperature for 1h, and then the reaction was cooled down. After this procedure, it was performed the same purification method commented above in the synthesis of MMNP1. Finally the NPs MMNP3 were suspended in toluene.

**Functionalization of MMNPs**

Detailed procedures concerning the synthesis of ligand are described in the supporting information. The functionalization was performed by a ligand exchange protocol previously described by us.[46]

**Physicochemical characterization**

**TEM.** Electron microscopy images were recorded on a FEI Tecnai G2 Twin microscope (accelerating voltage 100 kV). NPs samples for TEM analysis were prepared on a carbon-coated copper grid at a concentration of 1 g/L Fe. The diameters were calculated on an average of hundred NPs measured.

**ICP-HRMS.** Fe concentration was determined on an ICP-HRMS. Magnetic NPs were digested with aqua regia. Briefly, 2.5 mL of aqua regia were added to 25 µL of a solution of NPs in a volumetric flask. The mixture was left overnight. Then, milli-Q water was added to complete the total volume of 25 mL.

**DLS.** Size distribution and zeta potential of the gallol derived magnetic NPs were determined on a Zetasizer Nano ZS90 (Malvern, USA). The NPs were dispersed in milli-Q water, PBS or FBS at a concentration of 100 mg/L of Fe. Details on DLS measurements are provided in the supporting information.

**Magnetic Relaxivivities.** $r_2$ relaxivities were calculated at 1.44 T (Bruker Minispec) and 9.4 T (Bruker Biospec) using concentrations of magnetic NPs ranging between 0.1 and 2 mM of Fe under physiological conditions, at 37°C. $T_2$ was determined using acquisition schemes based on the Carl–Purcell–Meiboom–Gill (CPMG) sequence, either by spectroscopy (1.44 T) or imaging (9.4 T).

***In vitro* cell experiments**

**Cell Culture.** Mouse microglia cell line N13 were cultured in Roswell Park Memorial Institute medium (RPMI) supplemented with 10% fetal bovine serum (FBS), 2 mM L-glutamine, and 1% penicillin/streptomycin at 37 ºC in an incubator with 5% $CO_2$. Rat Glioblastoma cell line C6 were cultured in Dulbecco's Modified Eagle Medium (DMEM) supplemented with 10% fetal bovine serum (FBS), 2 mM L-glutamine, and 1% penicillin/streptomycin at 37 ºC in an incubator with 5% $CO_2$.

**Cytotoxicity assays.** Cytotoxicity was evaluated in N13 cells using the MTT assay, cell morphology studies and viable/necrotic/apoptotic assays, which are described in detail in the supporting information.

**Flow cytometry.** N13 cells were seeded overnight in 12-well plates (120.000 cells per well), in a total volume of 1 mL, and treated as described before. Then, cells were fixed in an ice-cold solution of 70% (v/v) ethanol for at least 24h, incubated for 10min in DNA extraction buffer (0.2 M $Na_2HPO_4$, pH 7.8) and then incubated with 0.1% (w/v) RNAse (Thermofisher,Waltham, MA, USA) and 50 µg/mL propidium iodide at 37 °C for 30min before analysis of the DNA content by flow cytometry using cell quest software (BD Biosciences, San Jose, CA, USA).

***In vivo* experiments**

Experiments involving animals followed the ethical guidelines of our local ethical committee and national regulations for the care and use of experimental animals (R.D. 53/2013, accreditation number 04/09/2018/132).

**Tumor implantation.** Male Wistar rat (8-week, 190 g, n = 3), provided by Janvier Labs, were used. C6 cells were brought to 80-90% confluence in culture. Then, cells were trypsinized and pelleted at 4 °C. The animals were anesthetized by intraperitoneal injection of a mixture of anesthetics (Buprenorphine / Medetomidine / Ketamine) and placed in the stereotactic apparatus. An incision was made in the skin, leaving the skull exposed, and a small perforation was performed 3.5 mm to the right of the bregma. $10^5$ cells were inoculated at 5.5 mm from the cranial surface, corresponding to the caudate nucleus.

**In vivo MRI.** Animals were anesthetized with 1% isoflurane, their tail vein cannulated, and then placed in the magnet. Vital constants, respiration and body temperature, were monitored throughout the entire experiment. Magnertic NPs were administered intravenously via tail vein at a concentration of 10 mg/kg Fe.

MRI experiments were conducted on a Bruker Biospec 9.4 T system. The acquisition scheme is described in detail in the supporting information. Short-term pharmacokinetics, corresponding to the first 30 min post-injection, were obtained by semi-quantitative analysis of a dynamic $T_2$-weighted image sequence. The average signal from regions of interest (ROIs) placed on the tumor was normalized to the average signal from ROIs placed on the contralateral brain tissue.

Then, to assess tumor vascularization and permeability, dynamic contrast-enhanced MRI (DCE-MRI) was performed following the intravenous injection of a commercial Gd chelate (Gadovist®) at a dose of 0.3 mmol/kg. These results were used to determine the viable (vascularized) and necrotic parts of the tumor, which were used for the short- and long-term pharmacokinetics analyses.

Finally, long-term pharmacokinetics were determined by quantitative $T_2$ mapping at 0, 1 and 24 h. According to the DCE-MRI experiments, $T_2$ values were calculated as the average within ROIs placed on the peripheral (vascularized) part of the tumor and over the entire tumo, as explained above.

Parametric $T_2$ and TTP maps were calculated with scripts written in-house in IDL (Interactive Data Language, Harris Geospatial Solutions, Inc., Broomfield, CO, USA).

**Histology.** Histology was evaluated at 24 h post MMNPs injection. Animals were sacrificed, and tumors and main organs were extracted. Histology was determined by light microscopy. Tissue

architecture was evaluated in H&E-stained tissue sections, while Prussian Blue staining was used to visualize iron deposits (for further details see the supporting information).

**Statistical analysis.** Statistical analysis was performed using the SPSS package (SPSS Inc., Chicago, Illinois). Cell viability and *in vivo* MRI data are shown as mean ± standard deviation (SD). Student's t-test or two-way analysis of variance were used to determine significant differences. The level of significance was $p<0.05$.

## Conclusions

The results presented here indicate that the EPR effect is a very inefficient mechanism to target brain tumors with metallic nanoparticles. On the one hand, our data indicate that the cutoff size of the BBTB is around 50 nm, impeding MMNPs above this size to reach the tumor interstitium passively. On the other hand, even for MMNPs around 30-50 nm and despite their long circulation times and high bioavailability, the amount of them found within the tumor was scarce and restricted to the surroundings of large tumor vessels. These findings add experimental evidence in favor of postulates that question the efficiency of the EPR effect to passively target nanoparticles to solid tumors, particularly brain tumors. Taken together, our results suggest that alternative mechanisms, such as active targeting, are needed for effective delivery of MMNPs to brain tumors.

## Author Contributions

M.P.L and M.L.G.M conceptualized the study, designed the methodology and acquired funding, C.C., A.A. and J.M.P.M. conducted the investigation, C.C. made the formal analysis and wrote the initial draft, M.L.G.M reviewed and edited the article to its final form. All authors have given approval to the final version of the manuscript.

## Conflicts of interest

There are no conflicts to declare.

## Acknowledgements

Financial support was provided by the Spanish Ministry of Economy, Industry and Competitiveness (CTQ2017-86655-R), the Spanish Ministry of Science and Innovation (PID2020-118448RB-C21 and PID2020-118448RB-C22), and by the Regional Ministry of Health of Andalusia (OH-0026-2018). The authors thank Roberto Gallardo for the development of the heater controller. The authors thank Juan F. López for assistance with the TEM studies, John Pearson for assistance with live-dead experiments, Luisa Macías for assistance with cell experiments, Reyes Molina for assistance with animal manipulations, Alejandro Dominguez for assistance with histology studies, and Maria Somoza for assistance with MRI experiments. TEM, Optical Microcopy, and MRI experiments were carried out in the ICTS "NANBIOSIS", specifically in the U28 Unit at the Andalusian Centre for Nanomedicine & Biotechnology (BIONAND).

## References

1. R. M. Young, A. Jamshidi, G. Davis and J. H. Sherman, *Annals of translational medicine*, 2015, **3**, 121.
2. A. Woehrer, L. Bauchet and J. S. Barnholtz-Sloan, *Current opinion in neurology*, 2014, **27**, 666-674.
3. D. Krex, B. Klink, C. Hartmann, A. von Deimling, T. Pietsch, M. Simon, M. Sabel, J. P. Steinbach, O. Heese, G. Reifenberger, M. Weller and G. Schackert, *Brain : a journal of neurology*, 2007, **130**, 2596-2606.
4. D. Nizamutdinov, E. M. Stock, J. A. Dandashi, E. A. Vasquez, Y. Mao, S. Dayawansa, J. Zhang, E. Wu, E. Fonkem and J. H. Huang, *World neurosurgery*, 2018, **109**, e67-e74.
5. R. Stupp, M. Brada, M. J. van den Bent, J. C. Tonn and G. Pentheroudakis, *Annals of oncology : official journal of the European Society for Medical Oncology*, 2014, **25 Suppl 3**, iii93-101.
6. J. E. Villanueva-Meyer, M. C. Mabray and S. Cha, *Neurosurgery*, 2017, **81**, 397-415.
7. Z. Zhou and Z. R. Lu, *Wiley Interdiscip Rev Nanomed Nanobiotechnol*, 2013, **5**, 1-18.
8. P. Caravan, J. J. Ellison, T. J. McMurry and R. B. Lauffer, *Chemical reviews*, 1999, **99**, 2293-2352.
9. T. Kanda, K. Ishii, H. Kawaguchi, K. Kitajima and D. Takenaka, *Radiology*, 2014, **270**, 834-841.
10. R. J. McDonald, J. S. McDonald, D. F. Kallmes, M. E. Jentoft, D. L. Murray, K. R. Thielen, E. E. Williamson and L. J. Eckel, *Radiology*, 2015, **275**, 772-782.
11. E. Lancelot, J. S. Raynaud and P. Desché, *Investigative radiology*, 2020, **55**, 578-588.
12. Y. Yan, X. Sun and B. Shen, *Oncotarget*, 2017, **8**, 43491-43505.
13. R. Stupp, M. E. Hegi, W. P. Mason, M. J. van den Bent, M. J. Taphoorn, R. C. Janzer, S. K. Ludwin, A. Allgeier, B. Fisher, K. Belanger, P. Hau, A. A. Brandes, J. Gijtenbeek, C. Marosi, C. J. Vecht, K. Mokhtari, P. Wesseling, S. Villa, E. Eisenhauer, T. Gorlia, M. Weller, D. Lacombe, J. G. Cairncross and R. O. Mirimanoff, *The Lancet. Oncology*, 2009, **10**, 459-466.
14. E. H. Chang, J. B. Harford, M. A. Eaton, P. M. Boisseau, A. Dube, R. Hayeshi, H. Swai and D. S. Lee, *Biochemical and biophysical research communications*, 2015, **468**, 511-517.
15. J. Shi, P. W. Kantoff, R. Wooster and O. C. Farokhzad, *Nature Reviews Cancer*, 2017, **17**, 20-37.
16. K. Kim and D. Khang, *Int J Nanomedicine*, 2020, **15**, 5719-5743.
17. E.-K. Lim, T. Kim, S. Paik, S. Haam, Y.-M. Huh and K. Lee, *Chemical reviews*, 2015, **115**, 327-394.
18. S. Swain, P. K. Sahu, S. Beg and S. M. Babu, *Current drug delivery*, 2016, **13**, 1290-1302.
19. Z. Yu, L. Gao, K. Chen, W. Zhang, Q. Zhang, Q. Li and K. Hu, *Nanoscale Research Letters*, 2021, **16**, 88.
20. S. Zhao, X. Yu, Y. Qian, W. Chen and J. Shen, *Theranostics*, 2020, **10**, 6278-6309.
21. A. Avasthi, C. Caro, E. Pozo-Torres, M. P. Leal and M. L. Garcia-Martin, *Top Curr Chem (Cham)*, 2020, **378**, 40.
22. Q. Zhou, C. Dong, W. Fan, H. Jiang, J. Xiang, N. Qiu, Y. Piao, T. Xie, Y. Luo, Z. Li, F. Liu and Y. Shen, *Biomaterials*, 2020, **240**, 119902.
23. Y. Matsumura and H. Maeda, *Cancer research*, 1986, **46**, 6387-6392.

24. S. Kunjachan, R. Pola, F. Gremse, B. Theek, J. Ehling, D. Moeckel, B. Hermanns-Sachweh, M. Pechar, K. Ulbrich, W. E. Hennink, G. Storm, W. Lederle, F. Kiessling and T. Lammers, *Nano letters*, 2014, **14**, 972-981.
25. H. Maeda, *Advanced drug delivery reviews*, 2015, **91**, 3-6.
26. H. Maeda, J. Wu, T. Sawa, Y. Matsumura and K. Hori, *Journal of controlled release : official journal of the Controlled Release Society*, 2000, **65**, 271-284.
27. C. Caro and D. Pozo, *Current pharmaceutical design*, 2015, **21**, 4822-4836.
28. Y. Yao, Y. Zhou, L. Liu, Y. Xu, Q. Chen, Y. Wang, S. Wu, Y. Deng, J. Zhang and A. Shao, *Frontiers in Molecular Biosciences*, 2020, **7**.
29. R. Lugano, M. Ramachandran and A. Dimberg, *Cell Mol Life Sci*, 2020, **77**, 1745-1770.
30. H. Cabral, Y. Matsumoto, K. Mizuno, Q. Chen, M. Murakami, M. Kimura, Y. Terada, M. R. Kano, K. Miyazono, M. Uesaka, N. Nishiyama and K. Kataoka, *Nature Nanotechnology*, 2011, **6**, 815-823.
31. H. Kang, S. Rho, W. R. Stiles, S. Hu, Y. Baek, D. W. Hwang, S. Kashiwagi, M. S. Kim and H. S. Choi, *Advanced Healthcare Materials*, 2020, **9**, 1901223.
32. D. Kalyane, N. Raval, R. Maheshwari, V. Tambe, K. Kalia and R. K. Tekade, *Materials Science and Engineering: C*, 2019, **98**, 1252-1276.
33. M. Longmire, P. L. Choyke and H. Kobayashi, *Nanomedicine (Lond)*, 2008, **3**, 703-717.
34. O. van Tellingen, B. Yetkin-Arik, M. C. de Gooijer, P. Wesseling, T. Wurdinger and H. E. de Vries, *Drug resistance updates : reviews and commentaries in antimicrobial and anticancer chemotherapy*, 2015, **19**, 1-12.
35. H. Sarin, A. S. Kanevsky, H. Wu, K. R. Brimacombe, S. H. Fung, A. A. Sousa, S. Auh, C. M. Wilson, K. Sharma, M. A. Aronova, R. D. Leapman, G. L. Griffiths and M. D. Hall, *Journal of translational medicine*, 2008, **6**, 80.
36. H. Sarin, A. S. Kanevsky, H. Wu, A. A. Sousa, C. M. Wilson, M. A. Aronova, G. L. Griffiths, R. D. Leapman and H. Q. Vo, *Journal of translational medicine*, 2009, **7**, 51.
37. K. E. Schlageter, P. Molnar, G. D. Lapin and D. R. Groothuis, *Microvascular research*, 1999, **58**, 312-328.
38. E. Blanco, H. Shen and M. Ferrari, *Nature Biotechnology*, 2015, **33**, 941-951.
39. K. Fabel, J. Dietrich, P. Hau, C. Wismeth, B. Winner, S. Przywara, A. Steinbrecher, W. Ullrich and U. Bogdahn, *Cancer*, 2001, **92**, 1936-1942.
40. T. Siegal, A. Horowitz and A. Gabizon, *Journal of neurosurgery*, 1995, **83**, 1029-1037.
41. J. Jin, K. H. Bae, H. Yang, S. J. Lee, H. Kim, Y. Kim, K. M. Joo, S. W. Seo, T. G. Park and D. H. Nam, *Bioconjug Chem*, 2011, **22**, 2568-2572.
42. S. Gelperina, O. Maksimenko, A. Khalansky, L. Vanchugova, E. Shipulo, K. Abbasova, R. Berdiev, S. Wohlfart, N. Chepurnova and J. Kreuter, *European Journal of Pharmaceutics and Biopharmaceutics*, 2010, **74**, 157-163.
43. S. Suárez-García, N. Arias-Ramos, C. Frias, A. P. Candiota, C. Arús, J. Lorenzo, D. Ruiz-Molina and F. Novio, *ACS Applied Materials & Interfaces*, 2018, **10**, 38819-38832.
44. M. Pernia Leal, C. Munoz-Hernandez, C. C. Berry and M. Garcia-Martin, *RSC Advances*, 2015, **5**, 76883-76891.
45. J. Park, K. An, Y. Hwang, J. G. Park, H. J. Noh, J. Y. Kim, J. H. Park, N. M. Hwang and T. Hyeon, *Nat Mater*, 2004, **3**, 891-895.
46. E. Pozo-Torres, C. Caro, A. Avasthi, J. M. Paez-Munoz, M. L. Garcia-Martin, I. Fernandez and M. Pernia Leal, *Soft Matter*, 2020, **16**, 3257-3266.
47. R. Stiufiuc, C. Iacovita, R. Nicoara, G. Stiufiuc, A. Florea, M. Achim and C. M. Lucaciu, *Journal of Nanomaterials*, 2013, **2013**, 146031.
48. C. Caro, D. Egea-Benavente, R. Polvillo, J. L. Royo, M. Pernia Leal and M. L. García-Martín, *Colloids and surfaces. B, Biointerfaces*, 2019, **177**, 253-259.
49. R. J. Deissler, M. A. Martens, Y. Wu and R. Brown, 2013.
50. M. Wu, H. Guo, L. Liu, Y. Liu and L. Xie, *Int J Nanomedicine*, 2019, **14**, 4247-4259.
51. C. Caro, M. Carmen Muñoz-Hernández, M. P. Leal and M. L. García-Martín, *Methods in molecular biology (Clifton, N.J.)*, 2018, **1718**, 409-419.
52. A. K. Heye, R. D. Culling, C. Valdes Hernandez Mdel, M. J. Thrippleton and J. M. Wardlaw, *Neuroimage Clin*, 2014, **6**, 262-274.
53. J. G. Smirniotopoulos, F. M. Murphy, E. J. Rushing, J. H. Rees and J. W. Schroeder, *RadioGraphics*, 2007, **27**, 525-551.
54. S. L. Barnes, J. G. Whisenant, M. E. Loveless and T. E. Yankeelov, *Pharmaceutics*, 2012, **4**, 442-478.
55. W. Xue, X. Du, H. Wu, H. Liu, T. Xie, H. Tong, X. Chen, Y. Guo and W. Zhang, *Sci Rep*, 2017, **7**, 13894.
56. J. W. Nichols and Y. H. Bae, *Journal of controlled release : official journal of the Controlled Release Society*, 2014, **190**, 451-464.
57. F. Danhier, *Journal of controlled release : official journal of the Controlled Release Society*, 2016, **244**, 108-121.
58. P. Guo, D. Liu, K. Subramanyam, B. Wang, J. Yang, J. Huang, D. T. Auguste and M. A. Moses, *Nat Commun*, 2018, **9**, 130.
59. Y. Hui, X. Yi, D. Wibowo, G. Yang, A. P. J. Middelberg, H. Gao and C.-X. Zhao, *Sci Adv*, 2020, **6**, eaaz4316-eaaz4316.
60. R. F. Barth and B. Kaur, *J Neurooncol*, 2009, **94**, 299-312.
61. S. Lope-Piedrafita, M. L. Garcia-Martin, J. P. Galons, R. J. Gillies and T. P. Trouard, *NMR in biomedicine*, 2008, **21**, 799-808.
62. H. B. Lee and M. D. Blaufox, *Journal of Nuclear Medicine*, 1985, **26**, 72-76.
63. C. D. Arvanitis, G. B. Ferraro and R. K. Jain, *Nat Rev Cancer*, 2020, **20**, 26-41.
64. J. W. Nichols and Y. H. Bae, *Nano Today*, 2012, **7**, 606-618.